

## Article

# Magnetic Properties of Bi-Magnetic Core/Shell Nanoparticles: The Case of Thin Shells

Alexander Omelyanchik <sup>1,2,\*</sup> , Silvia Villa <sup>1</sup>, Gurvinder Singh <sup>3</sup> , Valeria Rodionova <sup>2</sup> , Sara Laureti <sup>3</sup>, Fabio Canepa <sup>1</sup>  and Davide Peddis <sup>1,4,\*</sup>

<sup>1</sup> nM2-Laboratoire, Department of Chemistry and Industrial Chemistry, University of Genova, 16146 Genova, Italy; silvia.villa89@gmail.com (S.V.); fabio.canepa@unige.it (F.C.)

<sup>2</sup> REC “Smart Materials and Biomedical Applications”, Immanuel Kant Baltic Federal University, 236041 Kaliningrad, Russia; valeriarodionova@gmail.com

<sup>3</sup> Department of Biomedical Engineering and Sydney Nano Institute, The University of Sydney, Sydney, NSW 2008, Australia; gurvinder.singh@sydney.edu.au (G.S.); sara.laureti@ism.cnr.it (S.L.)

<sup>4</sup> nM2-Laboratoire, Consiglio Nazionale delle Ricerche, Istituto di Struttura della Materia, Monterotondo Scalo, 00015 Rome, Italy

\* Correspondence: asomelyanchik@kantiana.ru (A.O.); davide.peddis@unige.it (D.P.)

**Abstract:** Bi-magnetic core/shell nanoparticles were synthesized by a two-step high-temperature decomposition method of metal acetylacetonate salts. Transmission electron microscopy confirmed the formation of an ultrathin shell (~0.6 nm) of NiO and NiFe<sub>2</sub>O<sub>4</sub> around the magnetically hard 8 nm CoFe<sub>2</sub>O<sub>4</sub> core nanoparticle. Magnetization measurements showed an increase in the coercivity of the single-phase CoFe<sub>2</sub>O<sub>4</sub> seed nanoparticles from ~1.2 T to ~1.5 T and to ~2.0 T for CoFe<sub>2</sub>O<sub>4</sub>/NiFe<sub>2</sub>O<sub>4</sub> and CoFe<sub>2</sub>O<sub>4</sub>/NiO, respectively. The NiFe<sub>2</sub>O<sub>4</sub> shell also increases the magnetic volume of particles and the dipolar interparticle interactions. In contrast, the NiO shell prevents such interactions and keeps the magnetic volume almost unchanged.

**Keywords:** magnetic nanoparticles; exchange-coupling; magnetic volume; CoFe<sub>2</sub>O<sub>4</sub>; NiFe<sub>2</sub>O<sub>4</sub>; NiO



**Citation:** Omelyanchik, A.; Villa, S.; Singh, G.; Rodionova, V.; Laureti, S.; Canepa, F.; Peddis, D. Magnetic Properties of Bi-Magnetic Core/Shell Nanoparticles: The Case of Thin Shells. *Magnetochemistry* **2021**, *7*, 146. <https://doi.org/10.3390/magnetochemistry7110146>

Academic Editors:  
Sergey Borisovich Leble and  
Christina Gritsenko

Received: 17 September 2021  
Accepted: 29 October 2021  
Published: 8 November 2021

**Publisher's Note:** MDPI stays neutral with regard to jurisdictional claims in published maps and institutional affiliations.



**Copyright:** © 2021 by the authors. Licensee MDPI, Basel, Switzerland. This article is an open access article distributed under the terms and conditions of the Creative Commons Attribution (CC BY) license (<https://creativecommons.org/licenses/by/4.0/>).

## 1. Introduction

Bi-magnetic exchange coupled systems consisting of ferro(i)-/antiferromagnetic (F(i)M)/AFM) or magnetically hard/soft (h-FM/s-FM) materials provide enhanced magnetic properties compared to their individual counterparts (i.e., single-phase systems) [1–5]. AFM/FM systems may cause an increase of magnetic anisotropy, that is exploited in different applications such as recording media, spintronics and permanent magnets [3,6–8]. Aside from the Exchange Bias phenomenon, resulting in unidirectional exchange anisotropy, an increase of the effective anisotropy energy of the FM phase has also been observed in AFM/FM systems [8,9]. On the other hand, bi-magnetic systems consisting of two FM or FiM interfaced phases, such as h-FM/s-FM core/shell nanoparticles (NPs), with tunable saturation magnetization ( $M_S$ ), and magnetic anisotropy ( $K$ ) are beneficial to achieve, for example, contrast-enhanced magnetic resonance imaging or a high thermomagnetic effect [1,2,4,10–12]. Indeed, the magnetic properties of core/shell systems depend on the intrinsic parameters of h-FM and s-FM phases, as well as on the coupling strength and nanoparticle architecture which are controlled by the synthesis procedure (size of layers, quality of interface, shape, etc.) [4].

Depending on the size/thickness of h-FM and s-FM phases, the bi-magnetic system can act in a rigidly coupled regime if the s-FM phase is thinner than the double domain wall thickness of the h-FM [5]. This regime is characterized by a squared hysteresis loop of the soft phase being strongly exchange-coupled with the hard phase and the magnetization reversal process of the two phases occurring at the same field. In the case of the thicker s-FM phase, its reversal occurs at significantly lower fields than the switching of the h-FM. However, with regard to nanoparticles, a wider phenomenology may be observed due to

the large dispersion of magnetic properties arising from size distributions or divergences in the structural properties (i.e., stoichiometry and unit-cell parameters) of nanomaterials compared to bulk analog materials [13]. Special attention has been paid to the formation of the ultrathin shell of a few atomic layer thicknesses, exhibiting an enhanced spin canting (ESC) effect [14] which brings out a larger magnetic surface anisotropy, allowing exchange coupled systems to increase, for example, magnetic energy product  $(BH)_{\max}$  or specific loss power.

This paper discusses the effect of thin AFM and s-FiM shells on the magnetic properties of  $\text{CoFe}_2\text{O}_4$  nanoparticles. The cobalt ferrite is one of the most studied oxides with a spinel structure that presents (semi-)hard magnetic properties [15,16]. To tune its magnetic anisotropy, a thin shell ( $\sim 0.6$ -nm) of s-FiM- $\text{NiFe}_2\text{O}_4$  or AFM- $\text{NiO}$  has been deposited on the nanoparticle's surface. Both core/shell systems showed an increase of coercivity ( $H_C$ ) with an almost unchanged saturation magnetization compared to cobalt ferrite NPs.

## 2. Materials and Methods

### 2.1. Synthesis of NPs

Iron (III) acetylacetonate (97%), Cobalt (II) acetylacetonate (97%) and Nickel (II) acetylacetonate (95%) were purchased from Alfa Aesar (Kandel, Germany). Oleic acid (AO) (technical grade, 90%), Oleylamine (OLA) (technical grade, 70%), benzyl ether (99%), toluene, 2-propanol, and acetone were purchased from Sigma Aldrich (Darmstadt, Germany) and used without further purification. All the syntheses were conducted under oxygen-free conditions in a Schlenk line.

The single-phase core system was synthesized following a modified procedure reported elsewhere [17,18]. To synthesize the  $\text{CoFe}_2\text{O}_4$  core, (CFO sample),  $\text{Fe}(\text{acac})_3$  (2 mmol),  $\text{Co}(\text{acac})_2$  (1 mmol), 1,2-hexadecanediol (10 mmol), OA (6 mmol), OLA (6 mmol), and benzyl ether (20 mL) were mixed and magnetically stirred under a flow of nitrogen. The mixture was heated to 200 °C for 100 min (5 °C/min) and then heated to reflux at 300 °C (5 °C/min) for 60 min. The black-colored mixture was left to cool to room temperature overnight and washed with acetone, toluene and isopropanol.

A seed-mediated growth technique at high temperature was used to achieve the core/shell structure. For example, for  $\text{CoFe}_2\text{O}_4/\text{NiFe}_2\text{O}_4$  NPs (CFO/NFO sample), cobalt ferrite seeds were sonicated in 5 mL benzyl ether in the presence of OA (600  $\mu\text{L}$ ). Then, the suspension was added to the round bottom flask containing  $\text{Ni}(\text{acac})_2$  (0.33 mmol),  $\text{Fe}(\text{acac})_3$  (0.67 mmol), OA (600  $\mu\text{L}$ ) in benzyl ether (15 mL). After 1h vacuum at RT, the solution was heated to reflux at 290 °C (5 °C/min) under an Argon atmosphere and was then kept at this temperature for 30 min. A similar protocol was used to prepare the  $\text{CoFe}_2\text{O}_4/\text{NiO}$  NPs (CFO/NiO sample).

### 2.2. Morphostructural Properties

The X-ray diffraction (XRD) patterns were obtained from a Bruker DaVinci2 diffractometer (Bruker, MA, USA) with a  $\text{Cu K}\alpha$  ( $\lambda = 1.54056 \text{ \AA}$ ) source in the  $10^\circ$ – $75^\circ$   $2\theta$  range. Crystal phase identification was performed with QualX software. The mean size of crystallites,  $d_{\text{XRD}}$ , was calculated by using Scherrer's equation [19]:

$$d_{\text{XRD}} = 0.9 \frac{\lambda}{\beta \cos(\theta)}, \quad (1)$$

where  $\beta$  is the full width at half-maximum (FWHM) of the peaks of the corresponding reflections at  $2\theta$  geometry.

Scanning Transmission Electron Microscopy (STEM) Hitachi S5500, operating at 30 kV, was used to investigate the size distribution and morphology of the particles. The specimens for the TEM analyses were prepared by depositing one or a few drops of the sample

on 300 mesh copper carbon grids. The particle size distribution obtained by the TEM image analysis was fitted by normal and log-normal functions:

$$P = \frac{A}{\sigma_{\text{TEM}}\sqrt{2\pi}} \exp - \left[ \frac{1}{2} \left( \frac{D}{\sigma_{\text{TEM}} \langle d_{\text{TEM}} \rangle} \right)^2 \right]; \quad \text{—normal distribution} \quad (2)$$

$$P_l = \frac{A}{D\sigma_{\text{TEM}}\sqrt{2\pi}} \exp - \left[ \frac{\ln^2 \left( \frac{D}{\langle d_{\text{TEM}} \rangle} \right)}{2\sigma_{\text{TEM}}^2} \right], \quad \text{—log-normal distribution} \quad (3)$$

where  $\langle d_{\text{TEM}} \rangle$  is the mean value of particle diameter  $D$  (variable) and  $\sigma$  is its standard deviation.

### 2.3. Magnetic Properties

The DC magnetization measurements were performed by a Quantum Design superconducting quantum interference device (SQUID) magnetometer. The sample, in the form of a powder, was immobilized in epoxy resin to avoid the movement of the nanoparticles during the measurements. Hysteresis loops were obtained in the  $\pm 5$  T applied magnetic field range at different temperatures from 5 to 300 K. The value of saturation magnetization,  $M_S$ , was estimated from the Law of Approach to Saturation (LAS) by fitting the high-field region of hysteresis with the function

$$M = M_S \left( 1 - A/H - B/H^2 \right), \quad (4)$$

where  $A$  and  $B$  are free parameters [20].

The magnetization versus temperature measurements were performed using the zero-field-cooled  $M_{\text{ZFC}}(T)$  and field-cooled  $M_{\text{FC}}(T)$  protocols in a low measuring magnetic field of 2.5 mT [21,22].  $M_{\text{ZFC}}(T)$  magnetization was carried out by firstly cooling the sample from room temperature to 5 K in a zero magnetic field. Then, a small measuring magnetic field was applied and the  $M_{\text{ZFC}}(T)$  was measured during warming from 5 to 300 K, whereas  $M_{\text{FC}}(T)$  was recorded during the subsequent cooling.

For an assembly of non-interacting particles, the difference in  $M_{\text{FC}} - M_{\text{ZFC}}$  is related to the distribution of the anisotropy energy barriers [22–24]:

$$M_{\text{FC}} - M_{\text{ZFC}} \sim \alpha \int_{\Delta E_c}^{\infty} f(\Delta E_a) dE, \quad (5)$$

where  $\alpha$  is a parameter proportional to the initial susceptibility of non-relaxing particles, measuring field and time;  $\Delta E_c$  is a critical value of energy, above which the particles are blocked. In other words,  $\Delta E_c = KV = 25k_B T_B$ , thus, Equation (5) shows the distribution of blocking temperatures:

$$f(T_B) \sim \frac{d(M_{\text{FC}} - M_{\text{ZFC}})}{dT}. \quad (6)$$

The  $f(\Delta T_B)$  can be fitted by a (log-)normal function because  $T_B$  is proportional to the particle volume, which is well-described by a (log-)normal function of the particle size distribution (Equations (2) and (3)) [22,25,26]; for the determination of  $T_B$  in the case of unmerged ZFC/FC, the  $d(M_{\text{FC}} - M_{\text{ZFC}})/dT$  is fitted by the normal function, then the average  $\langle T_B \rangle$  is determined as a temperature at which  $d^2(M_{\text{FC}} - M_{\text{ZFC}})/dT^2 = 0$ , to the left of the  $M_{\text{ZFC}}$  peak position [24].

## 3. Results

### 3.1. Morphostructural Properties

The XRD patterns suggest the presence of only spinel and rock salt phases in the bi-magnetic core/shell NPs (Figure 1a). No extra phases have been detected. Scanning transmission electron microscopy (STEM) images show a nearly spherical core and

core/shell NPs (Figure 1b), for which the mean diameter ( $d_{\text{TEM}}$ ) has been evaluated using Equations (2) and (3) by counting more than 200 NPs.

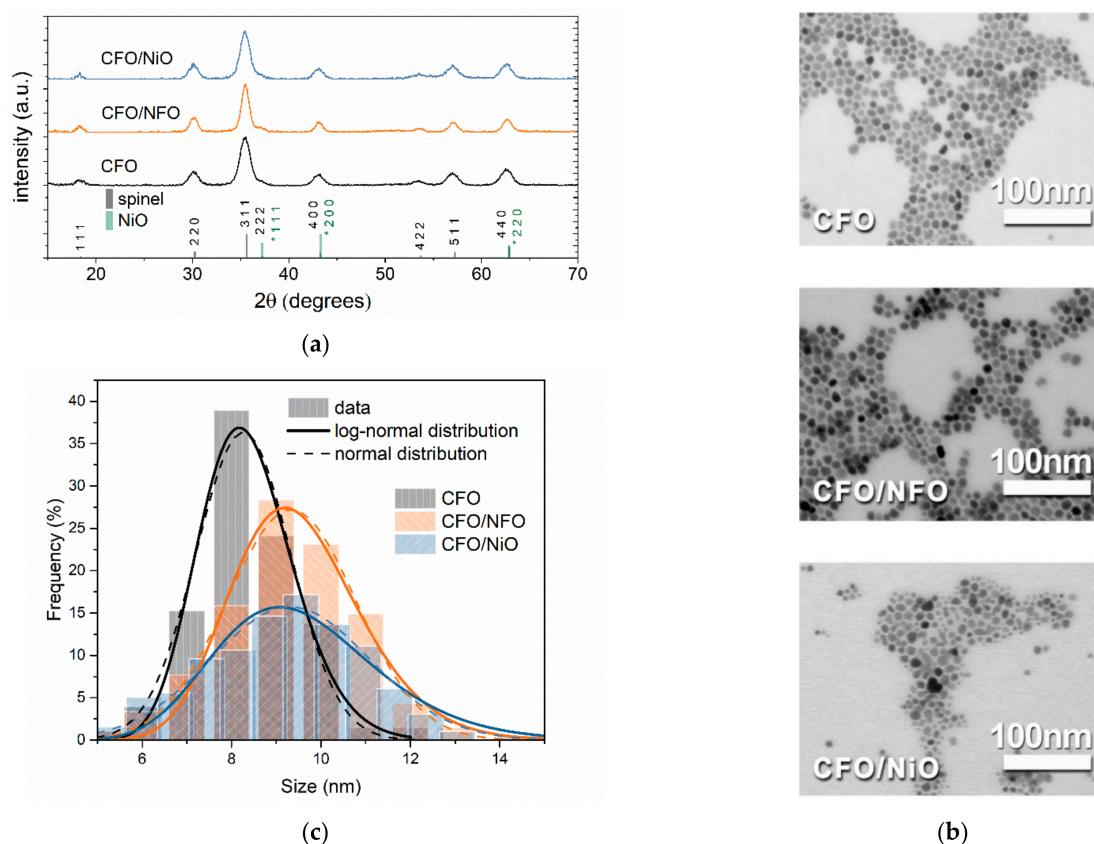


**Figure 1.** (a) XRD patterns and (b) STEM images for CFO seeds and core/shell systems; (c) diameter distribution obtained from STEM images.

On the other hand, the mean crystallites' size ( $d_{\text{XRD}}$ ), has been calculated using Equation (1) by averaging 5 the most intense XRD reflections. The size of the XRD and STEM measurements, reveals an increase in the diameter after the deposition of a thin shell around the CFO seed NPs, thus confirming the formation of core/shell structures (Figure 1c and Table 1). In particular, the size increase of the  $d_{\text{XRD}}$  for the CFO/NiO samples is found to be less than the size increase of the  $d_{\text{XRD}}$  for the CFO/NFO sample. This can probably be ascribed to the partial mismatch of spinel phase planes of the  $\text{CoFe}_2\text{O}_4$  with those of the rock salt structure of the NiO phase. However, the  $d_{\text{TEM}}$  values confirm the growth of a thin shell ( $\sim 0.6$  nm) in both core/shell systems, thus indicating a similar increase in the physical size for both systems. In all cases, these core/shell NPs exhibit a narrow size distribution characterized by the low values of the standard deviation  $\sigma_{\text{TEM}}$  of the log-normal distribution; the formation of a NiO shell induces a slightly higher dispersion with respect to the CFO/NFO sample (Table 1).

**Table 1.** Morpho-structural properties of samples: crystallite size ( $d_{\text{XRD}}$ ), particle size ( $d_{\text{TEM}}$ ) and standard deviation of the particle size distribution ( $\sigma_{\text{TEM}}$ ) after fit with normal and log-normal functions.

Sample	$d_{\text{XRD}}$ , nm	Normal		Log-Normal	
		$d_{\text{TEM}}$ , nm	$\sigma_{\text{TEM}}$	$d_{\text{TEM}}$ , nm	$\sigma_{\text{TEM}}$
CFO	$7.2 \pm 0.4$	$8.3 \pm 0.1$	$0.25 \pm 0.03$	$8.3 \pm 0.1$	$0.13 \pm 0.02$
CFO/NFO	$8.9 \pm 0.9$	$9.3 \pm 0.1$	$0.31 \pm 0.03$	$9.5 \pm 0.1$	$0.15 \pm 0.02$
CFO/NiO	$7.8 \pm 0.7$	$9.3 \pm 0.1$	$0.38 \pm 0.03$	$9.6 \pm 0.2$	$0.19 \pm 0.02$

Error for  $d_{\text{XRD}}$  is the standard deviation over values for all peaks; the error for  $d_{\text{TEM}}$  and  $\sigma_{\text{TEM}}$  is the error of fitting with normal and log-normal functions.

### 3.2. Magnetic Anisotropy

The temperature dependence of magnetization, which was investigated by the ZFC/FC protocol, shows the typical behavior of single-domain magnetic nanoparticles (Figure 2a). In all samples,  $M_{ZFC}$  and  $M_{FC}$  show irreversibility in the entire explored temperature range. Nevertheless, the average blocking temperature  $\langle T_B \rangle$ , which is determined as the temperature at which the magnetic anisotropy energy distribution  $f(\Delta E_a)$  reaches 50% (Figure 2b), is below 300 K. To define this value, we performed an extrapolation of the experimental data with the normal function fit following the procedure explained in p.2.3. In the literature, the log-normal distribution is mainly used to describe uncentered distributions of particle size [27]. The distribution of particle sizes is reflected in a log-normal distribution of the magnetic anisotropy energy barriers  $f(\Delta E_a) \sim KV$  [22,25,26]. However, in our case, the best fit of  $f(\Delta E_a)$  was achieved with the center-symmetrical normal distribution (Figure 2b). This may be attributed to the specific particle growth process. Fitting the particle size distribution with both Equations (2) and (3) provided similar results. Furthermore,  $f(\Delta E_a)$  is proportional to the particle volume but not to the diameter [28]. The volumetric distribution is three-times higher, thus it is expected  $\sigma_{MAG} = 3\sigma_{TEM}$ , where  $\sigma_{MAG}$  is the standard deviation of the magnetic anisotropy distribution  $f(\Delta E_a)$  [21]. The average value of the blocking temperature  $\langle T_B \rangle$  was found to be  $\sim 200$  K for the CFO and CFO/NiO samples, while it is significantly higher than the value of  $\sim 260$  K for the CFO/NFO samples (Table 2).

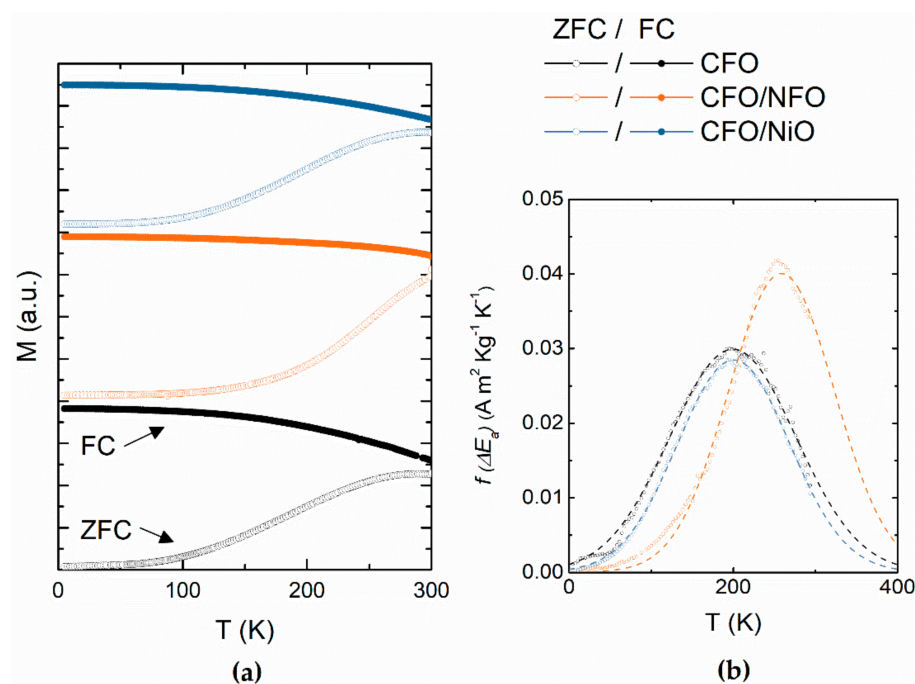


**Figure 2.** (a) Zero-field cooling and field cooling (ZFC/FC) magnetizations recorded in 2.5 mT measuring field; (b) distribution of magnetic anisotropy energy: measured (dots) and extrapolated by fit with the normal function (dashed lines).

**Table 2.** Mean value of blocking temperature ( $\langle T_B \rangle$ ) and its dispersion ( $\sigma_{MAG}$ ), saturation magnetization ( $M_S$ ), reduced remanent magnetization ( $M_R/M_S$ ) and coercivity field ( $\mu_0 H_C$ ).

Sample	$\langle T_B \rangle$ , K	$\sigma_{mag}$	$M_S$ , Am <sup>2</sup> kg <sup>-1</sup>	$M_R/M_S$	$\mu_0 H_C$ , T
CFO	201 ± 8	0.76 ± 0.05	84 ± 4	0.61 ± 0.01	1.2 <sup>1</sup>
CFO/NFO	259 ± 10	0.50 ± 0.05	75 ± 4	0.76 ± 0.01	1.5 ± 0.1
CFO/NiO	200 ± 8	0.65 ± 0.05	80 ± 4	0.74 ± 0.01	2.0 ± 0.1

<sup>1</sup> Error for this value is lower than reported significant digits.

Considering the Stoner–Wohlfarth model, the temperature dependence of coercivity can be expressed as follows:  $H_C = \zeta 2K/M_S [1 - (T/T_B)^{1/2}]$ , where  $\zeta$  is a coefficient, depending on the type of magnetic anisotropy and distribution of anisotropy axes (for an assembly of non-interacting randomly distributed magnetic particles with a dominating uniaxial anisotropy  $\zeta = 0.48$ ) [23]. Thus, at temperatures above  $T_B$ , all samples exhibit non-hysteretic behavior confirming the superparamagnetic state at 300 K (inset of Figure 3). M-H hysteresis loops recorded at 5 K show a typical shape for h-F(i)M magnetic material with a high value of both the coercivity ( $\mu_0 H_C$ ) and the reduced remanent magnetization ( $M_R/M_S$ ) for all samples (Figure 3 and Table 2). The one-step hysteresis loop confirms the rigid exchange coupling between the core and the shell phases. The values of saturation magnetization ( $M_S$ ) at 5 K extrapolated using Equation (4) are listed in Table 2. The highest value of  $M_S$  was found in the CFO sample ( $\sim 84 \text{ Am}^2/\text{kg}$ ) while the value of  $M_S$  was slightly reduced for both core/shell samples. Overall, the magnetic properties, in terms of  $M_S$ ,  $\mu_0 H_C$  and  $\langle T_B \rangle$ , that were observed for the CFO single-phase system are close to those previously reported for an  $\sim 8\text{-nm}$  [29] and  $\sim 7.5\text{-nm}$  [30]  $\text{CoFe}_2\text{O}_4$  NPs prepared using the high-temperature decomposition method.

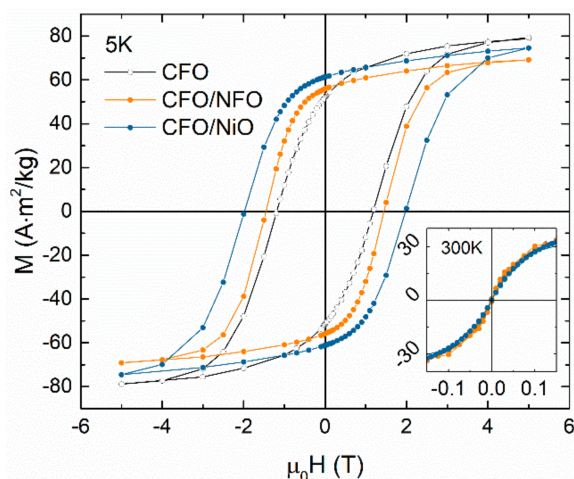


**Figure 3.** M-H hysteresis loop at 5 K for all samples. Inset shows low field region of M-H loops at 300 K.

Notably, both core/shell samples showed increased  $\mu_0 H_C$  values, i.e., 1.5 and 2.0 T for CFO/NFO and CFO/NiO, respectively, compared to the CFO sample ( $\mu_0 H_C = 1.2 \text{ T}$ ). An enhancement of the coercive field in exchange-coupled nanostructures, consisting of NiO AFM with h-FM CoPt [8] or h-FiM  $\text{CoFe}_2\text{O}_4$  [31] counterparts, had already been observed and was attributed to the interface exchange interaction. Moon et al. showed an increase of the anisotropy of h-FiM  $\text{CoFe}_2\text{O}_4$  covered with the ultrathin  $\text{NiFe}_2\text{O}_4$ ,  $\text{MnFe}_2\text{O}_4$  and  $\text{Fe}_3\text{O}_4$  s-FiM shells with a shell volume fraction ( $f_{\text{shell}} = V_{\text{shell}}/V_{\text{total}}$ ) lower than 0.25 [14]. This effect was attributed to an enhanced spin canting (ESC) regime of the surface. Indeed, the cobalt ions with the high anisotropy are found to have been less subjected to the canting, while in softer ferrites the spin canting may be stronger [32,33]. According to the literature, the surface and interface terms contribute to the uniaxial magnetic anisotropy of magnetic NPs [34–36]. In this case, the surface/interface effects in both core/shell systems demonstrated a tendency towards cubic anisotropy with  $M_R/M_S$  value of around 0.75, which is close to the theoretical value of  $\sim 0.8$ , while in the case of the uniaxial anisotropy, the lower value of  $\sim 0.5$  is expected [20].

A typical fingerprint of exchange-coupled AFM/F(i)M systems with the Néel temperature ( $T_N$ ) of an AFM phase below that of the Curie (Néel) temperature ( $T_C$ ) of an F(i)M phase is the horizontal shift of the hysteresis cycle (i.e., Exchange Bias) that may be observed under specific conditions [37,38]. Indeed, in a typical experiment to induce a preferential orientation of interface anisotropy, the material is cooled in the presence of a

saturation magnetic field from a temperature of above  $T_N$  to lower temperatures. Indeed, in the  $T_N < T < T_C$  temperature range, the AFM phase is in the paramagnetic state while F(i)M spins are aligned along the direction of the external magnetic field; according to the classical phenomenological description of the Exchange Bias phenomena [6], when cooling down to  $T < T_N$ , the AFM interface spins become aligned due to the exchange interaction with the F(i)M spins. At low temperatures, interfacial spins are pinned along the field cooling direction and act as a torque, thereby inducing a preferential direction to the magnetization of the F(i)M phase with a resulting horizontal shift of the hysteresis loop. In the case of the NiO AFM phase, although the  $T_N$  is relatively high (525 K), the loop shift can often be observed even after cooling from a temperature in the range of 300–380 K [8,32,39,40]. This result is explained as an effect of the disordered spins anchored at the interface as follows: since those spins are frustrated, their freezing occurs within a large temperature range which depends on the distribution of the anisotropy energy barrier; such a distribution depends on the local surroundings and the resulting freezing temperature can be significantly lower than the bulk  $T_N$  [38]. Nevertheless, in our systems, M-H cycles measured at 5 K after cooling from room temperature in a magnetic field of 3 T do not show any exchange bias shift (data are not presented). This can be explained as a result of an extremely thin AFM shell ( $t_{\text{shell}} \sim 0.6$  nm) that is not able to maintain the antiferromagnetic order, as well as due to a possible divergence in the stoichiometry of the shell material [13]. However, the core/shell exchange coupling of CFO/NiO nanoparticles leads to an increase of the effective anisotropy at 5 K.

### 3.3. Intra- and Interparticle Interactions

The effect of interparticle interactions was studied via a remanence plot technique by collecting the values of the remanent magnetization versus the external applied magnetic field  $\mu_0 H_{\text{app}}$  obtained from two different initial states of the sample, i.e.: (i) being demagnetized ( $m_R$ ) and (ii) being saturated in the negative field ( $m_D$ ) [41,42]. The  $m_R(H_{\text{app}})$  curve was obtained beginning with a demagnetized sample by applying a positive field  $\mu_0 H_{\text{app}}$ , which was then removed, and the remanence  $m_R(H_{\text{app}})$  was measured; the process was repeated after increasing the field of  $\mu_0 H_{\text{app}}$  up to +5 T (Figure 4a). Similarly, the  $m_D(H_{\text{app}})$  curve was measured by saturating the sample in a field of +5 T and then measuring the remanence  $m_D(H_{\text{app}})$  after applying a gradually increasing reverse field of  $\mu_0 H_{\text{app}}$  up to −5 T.

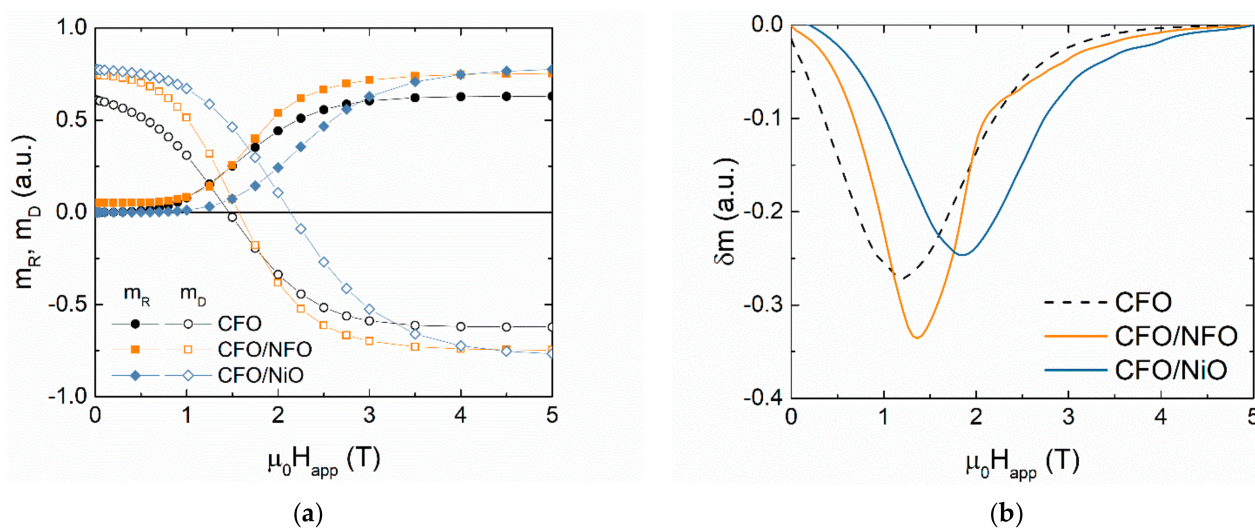


Figure 4. (a)  $m_R$  and  $m_D$  remanent magnetizations and (b)  $\delta m$ -plots for CFO, CFO/NFO and CFO/NiO systems at 5 K.

For a non-interacting assembly of uniaxial single-domain magnetic particles,  $m_R(H_{app})$  and  $m_D(H_{app})$  are connected according to the Wohlfarth model [43]. To quantify the level of interparticle interactions, the Kelly plot was used [44]:

$$\delta m = m_D - (1 - 2 \cdot m_R) \quad (7)$$

where the peak value of the  $\delta m(H_{app})$  function can be considered as a quantitative parameter of interparticle interactions ( $\delta m = 0$  for the ideal, non-interacting case). This method was extended to the case of particles characterized by a cubic anisotropy [42].

A negative value of  $\delta m$  indicates the dominant role of dipolar interactions among particles (Figure 4b). The higher magnitude of  $|\delta m|$  observed in CFO/NFO NPs may be attributed to the greater size of the particles compared to the CFO seeds. For CFO/NiO NPs the value of  $|\delta m|$  was the lowest among all samples because the AFM shell prevents the interactions among the FiM cores, by increasing the average core-to-core distance  $l$  (dipolar field  $\propto M_S^2 V^2 l^{-3}$ ), in agreement with the previously observed decrease of  $|\delta m|$  in the nanocomposite of the  $CoFe_2O_4$  and NiO NPs [31].

To further disclose the effect of the thin shell on the magnetic behavior of the NPs, the “magnetic size” of the particles was studied using three different approaches:

- I. Activation volume through magnetic viscosity coefficient [12,45,46];
- II. Fit of superparamagnetic M-H curve with Langevin–Chantrell method [47];
- III. Fit of superparamagnetic M-H curve with numerical inversion method [48,49].

The magnetic viscosity coefficient was found through the following relaxation measurements [12,32,46]: the sample was cooled down to 5 K; the sample was saturated in the magnetic field of  $-5$  T; a positive field ( $\mu_0 H_{app}$ ) was applied and magnetization as a function of time  $t$  was recorded during 120 min. In this way, a set of  $M(t)$  curves was obtained at different  $\mu_0 H_{app}$  around the coercivity field of the irreversible component of magnetization  $m_D$  ( $\mu_0 H_{CR}$ ) [26,50]. The  $\mu_0 H_{CR}$  values were defined as fields at which  $m_D(H_{app})$  crosses zero and were found to be  $\sim 1.5$ ,  $1.6$  and  $2.1$  T for CFO, CFO/NFO and CFO/NiO, respectively (the same fields corresponding to maximum position of  $dm_D/dH_{app}$ ). A logarithmic character for  $M(t)$  was also observed (Figure 5a):

$$M(t) = const \pm S \ln\left(\frac{t}{t_0}\right), \quad (8)$$

where  $S$  is the magnetic viscosity coefficient and  $t_0$  is the reference time. The descending slope of  $M(t)$  changes to ascending when the  $\mu_0 H_{app}$  reaches the value  $\sim \mu_0 H_{CR}$  (Figure 5b).

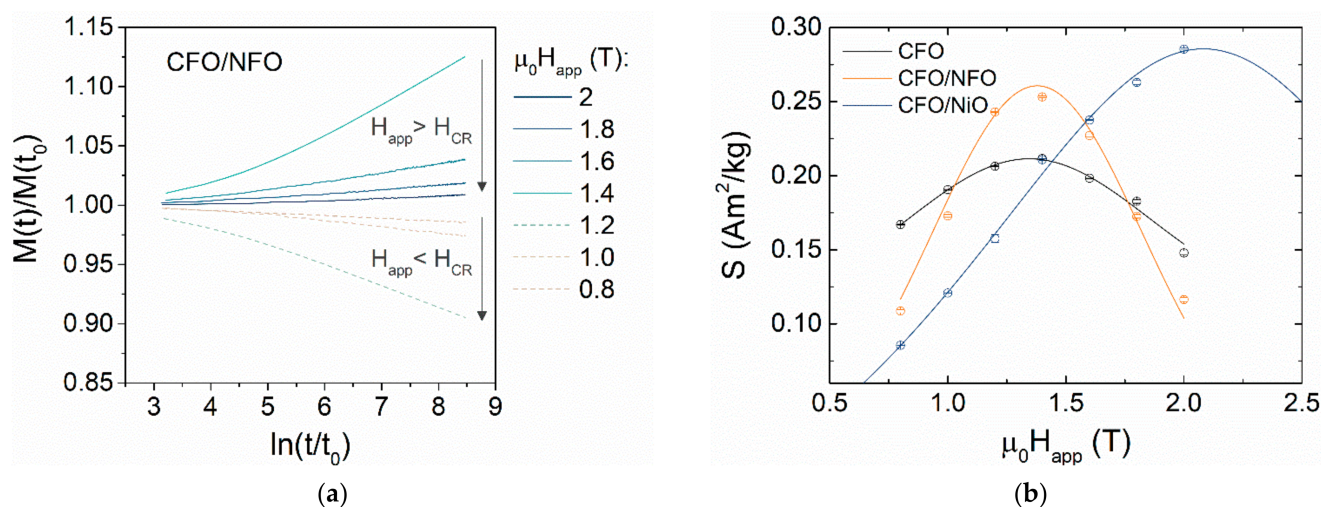


**Figure 5.** (a) normalized  $M(t)$  measured at different values of  $\mu_0 H_{app}$  after saturation at  $-5$  T for CFO/NFO sample; (b) magnetic viscosity  $S$  as a function of the applied field  $\mu_0 H_{app}$  for all samples.

According to the Néel theory [51], the fluctuation field ( $\mu_0 H_f$ ) is defined as  $\mu_0 H_f = S/\chi_{irr}$ , where  $\chi_{irr}$  is the irreversibility susceptibility, defined as a peak value of the first derivative  $M_S \times (dm_D/dH_{app})$ . This field describes the effect of the thermal fluctuations on magnetization reversal processes, leading to an equilibrium thermodynamic state. Based on this concept, the magnetic activation volume ( $V_{act}$ ) was defined as a volume of magnetic material involved in the process of overcoming the energy barrier for magnetization reversal. For single-domain particles with uniaxial anisotropy,  $V_{act}$  is:

$$V_{act} = \frac{k_B T \chi_{irr}}{M_S S}, \quad (9)$$

where  $k_B$  is the Boltzmann constant. In the case of the dominating cubic anisotropy, the magnetic particles have three easy axes and thus the energy barrier separating the minimums of the potential energy of magnetization states is lower than in the case of uniaxial anisotropy. It was shown in the first approximation that  $V_{act}^{cubic} = 4 \times V_{act}^{uniaxial}$  [46]. Following this procedure and considering the dominant cubic anisotropy, the activation volumes were found to be comparable to the expected values for all the samples; the magnetic volume of the seeds of CFO and CFO/NiO was equal within the experimental error, while it was larger for the CFO/NFO system. As shown in Table 3,  $V_{act}$  was converted into a "magnetic size"  $d_{mag}^I$  accounting for the spherical shape of particles. For a weakly interacting particles system, the magnetic size is expected to be equal to the physical size of the particles as estimated by the TEM analysis.

**Table 3.** Physical particle size determined from TEM analysis after log-normal fit ( $d_{TEM}^{log}$ ), magnetic size from the magnetic viscosity ( $d_{MAG}^I$ ), Langevin–Chantrell fit ( $d_{MAG}^{II}$ ) and MINORIM software ( $d_{MAG}^{III}$ ), standard deviation of log-normal distribution of physical ( $\sigma_{TEM}^{log}$ ) and magnetic ( $\sigma_{MAG}^{II}$ ) size.

Sample	$d_{TEM}^{log}$ , nm	$d_{MAG}^I$ , nm	$d_{MAG}^{II}$ , nm	$d_{MAG}^{III}$ , nm	$\sigma_{TEM}^{log}$	$\sigma_{MAG}^{II}$
CFO	$8.3 \pm 0.1$	$6.9 \pm 0.2$	$5.5 \pm 0.2$	6.9	$0.13 \pm 0.02$	$0.22 \pm 0.02$
CFO/NFO	$9.5 \pm 0.1$	$7.3 \pm 0.2$	$6.0 \pm 0.2$	7.7	$0.15 \pm 0.02$	$0.20 \pm 0.02$
CFO/NiO	$9.6 \pm 0.2$	$6.5 \pm 0.5$	$5.4 \pm 0.2$	6.9	$0.19 \pm 0.02$	$0.23 \pm 0.02$

Additionally, a determination of the magnetic size was performed by the fit of the superparamagnetic M-H curves with a Langevin function [52]:

$$\frac{M(H)}{M_S^b} = \coth\left(\frac{VM_S^b H}{k_B T}\right) - \frac{k_B T}{VM_S^b H}, \quad (10)$$

where  $M_S^b$  is the saturation magnetization of bulk material. In the Langevin–Chantrell method [47],  $V$  is considered to follow a log-normal distribution (Equation (3) with the appropriate replacement of size to volume or magnetic moment variables). The implementation of the fit procedure using Equation (10), with the substituted variable of the particle volume to its distribution, provides the magnetic size  $d_{mag}^{II}$  with its standard deviation  $\sigma_{mag}^{II}$  of the log-normal distribution. The fitted M-H curves at 300 K are presented in Figure 6.

An approach proposed to fit M-H is based on the numerical inversion method using the MINORIM software [49]. This method is also based on the fit of the M-H superparamagnetic curve with Equation (10) but does not assume a particular shape of the particle size distribution. To perform the fit for the CFO/NFO sample, an averaged value of  $M_S^b$  for both  $CoFe_2O_4$  and  $NiFe_2O_4$ , with regard to their content, has been considered. In the case of the fitting of the magnetization curve of the CFO/NiO sample, the value of  $M_S^b$  of the bulk  $CoFe_2O_4$  was obtained, considering that only the core contributes to the magnetization (Table 3).

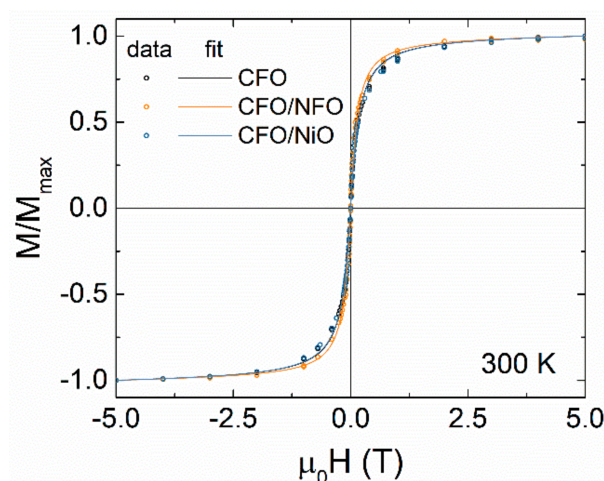


**Figure 6.** Measured and fitted with the Langevin–Chantrell method M-H cycles at 300 K.

By comparing the results from three different methods for the estimation of the magnetic size, a qualitative agreement among the three methods can be observed. The magnetic size increases when the h-FM CFO seeds are covered with the s-FiM NFO shell, while it remains the same in the case of an AFM NiO shell. Moreover, the magnetic size determined through magnetic viscosity was in better quantitative agreement with the result obtained from the numerical inversion method. This fact can be attributed to the non-log-normal distribution of the magnetic properties of the investigated samples. All the magnetic sizes are slightly lower than the physical particle sizes, which can be related to the following surface effects: disordered spins on the surface form a non-magnetic shell with a thickness in the range of 0.5–1 nm or some internal spin canting.

#### 4. Conclusions

A two-step seed-mediated thermal decomposition strategy was employed to fabricate bi-magnetic core/shell CFO/NFO and CFO/NiO NPs. The deposition of an ultrathin layer of ~0.6 nm NFO (s-FiM) and NiO (AFM) on ~8 nm CFO (h-FiM) seed particles strongly affected the magnetic reversal process of core/shell NPs. Both of the shells increased in their magnetic anisotropy and prevented reversible processes (residual thermal fluctuations) at low temperatures. The coercive field increased from ~1.2 T (CFO sample) to ~1.5 T for CFO/NFO and to ~2.0 T for CFO/NiO. The increased anisotropy results from the interface exchange interaction between the FiM core and AFM shell (CFO/NiO) or the disordered spins in the ESC regime (CFO/NFO). Nevertheless, the  $M_R/M_S$  ratio increases from ~0.61 for CFO to ~0.75 for core/shell samples, suggesting that the cubic-type magnetocrystalline anisotropy of the cobalt ferrite core is stabilized by the presence of the thin shell.

A more accurate description of the magnetic structure of synthesized particles was obtained via an analysis of the magnetic size of the particles, determined by three alternative approaches (i.e., magnetic viscosity, Langevin–Chantrell and numerical inversion methods). The magnetic size of the CFO seeds was slightly lower than the physical size, suggesting the presence of canted spins on the surface. In the CFO/NiO sample, the magnetic size was unaltered while the physical diameter increased (Figure 7). Thus, the AFM material on the particle's surface is not involved in the magnetization reversal processes, but, due to the strong exchange coupling, it strengthens the anisotropy and stabilizes the spins of the core against the thermal fluctuations. The increase in the magnetic size of the CFO/NFO sample confirms the coupling of the FiM shell spins with the core, while the shell affects the ESC regime, and increases the effective magnetic anisotropy. The s-FiM material of the  $\text{NiFe}_2\text{O}_4$  shell is more affected by the magnetic frustration than the effect of the frustration in the h-FiM material of the core.  $\text{Co}^{2+}$  ions with stronger single-ion anisotropy are less subjected to the canting than  $\text{Fe}^{3+}$  and  $\text{Ni}^{2+}$  with the lower anisotropy energy [32].

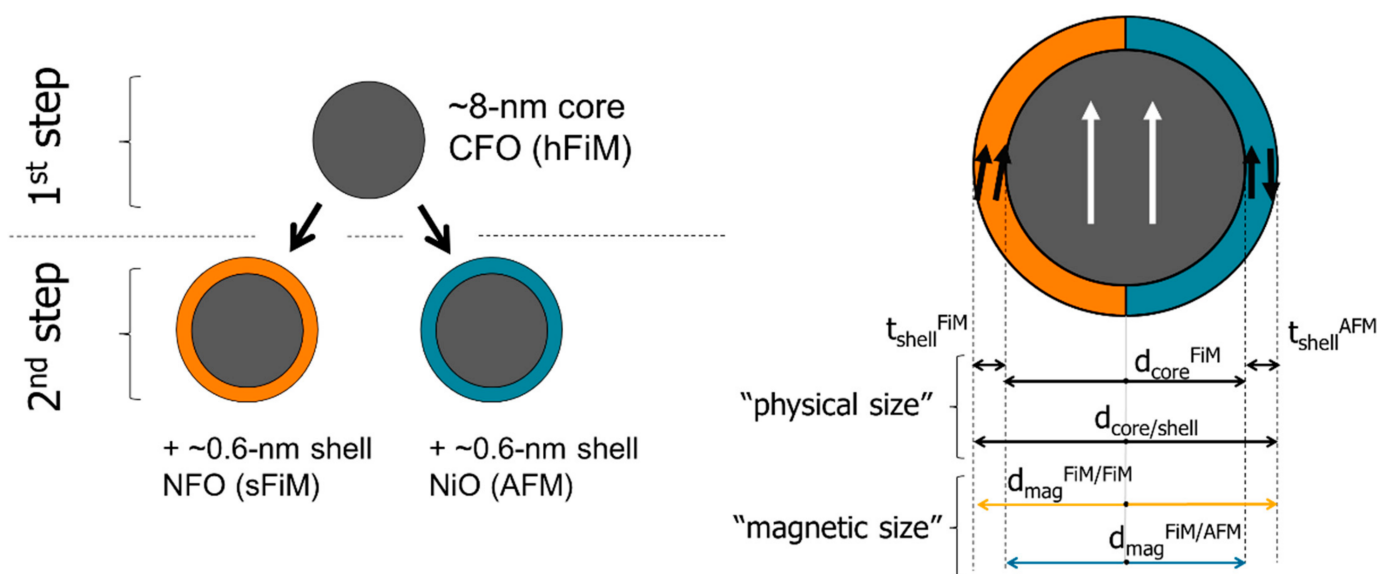


**Figure 7.** Schematic representation of the magnetic structure of CFO/NFO and CFO/NiO core/shell samples.

Interestingly, despite the very low thickness, the presence of different shells can affect not only single-particle behavior but also has a notable effect on the interparticle interaction strength. Indeed, the s-FiM shell increases the negative value of  $\delta m$ , suggesting a higher impact of the dipolar interactions, while the NiO shell prevents such interactions. The  $\langle T_B \rangle$  of the CFO/NiO sample was approximately equal to that of the CFO; however, given that it is proportional to the anisotropy barrier ( $\langle T_B \rangle \propto KV$ ), and considering that both systems have the same magnetic size, one expects the higher  $\langle T_B \rangle$  value for the sample with the higher anisotropy. This can be attributed to the significant effect of temperature on the interface component of magnetic anisotropy as well as the effect of interparticle interactions on the anisotropy energy barrier.

**Author Contributions:** Conceptualization, A.O. and D.P.; methodology, S.V., G.S., D.P., F.C., V.R.; validation, D.P., S.L. and F.C.; formal analysis, D.P., S.L. and F.C.; investigation, A.O., S.V., G.S. and D.P.; resources, D.P. and F.C.; data curation, D.P. and A.O.; writing—original draft preparation, A.O.; writing—review and editing, D.P., S.L. and G.S.; visualization, A.O.; supervision, D.P., F.C. and V.R.; project administration, D.P.; funding acquisition, D.P. All authors have read and agreed to the published version of the manuscript.

**Funding:** This work was partially supported by the European Union’s Horizon 2020 Research and Innovation Programme: under grant agreement No. 731976 (MAGENTA). A.O., V.R. and D.P. gratefully acknowledge the financial support of the Russian Science Foundation grant No. 21-72-30032 (magnetic measurements).

**Conflicts of Interest:** The authors declare no conflict of interest.

## References

- Lee, J.-H.; Jang, J.; Choi, J.; Moon, S.H.; Noh, S.; Kim, J.; Kim, J.-G.; Kim, I.-S.; Park, K.I.; Cheon, J. Exchange-coupled magnetic nanoparticles for efficient heat induction. *Nat. Nanotechnol.* **2011**, *6*, 418–422. [[CrossRef](#)] [[PubMed](#)]
- Noh, S.; Moon, S.H.; Shin, T.-H.; Lim, Y.; Cheon, J. Recent advances of magneto-thermal capabilities of nanoparticles: From design principles to biomedical applications. *Nano Today* **2017**, *13*, 61–76. [[CrossRef](#)]
- Vasilakaki, M.; Trohidou, K.N.; Nogués, J. Enhanced magnetic properties in antiferromagnetic-core/ferrimagnetic-shell nanoparticles. *Sci. Rep.* **2015**, *5*, 1–7. [[CrossRef](#)] [[PubMed](#)]
- Sanna Angotzi, M.; Mameli, V.; Cara, C.; Musinu, A.; Sangregorio, C.; Niznansky, D.; Xin, H.L.; Vejpravova, J.; Cannas, C. Coupled hard-soft spinel ferrite-based core-shell nanoarchitectures: Magnetic properties and heating abilities. *Nanoscale Adv.* **2020**, *2*, 3191–3201. [[CrossRef](#)]
- López-Ortega, A.; Estrader, M.; Salazar-Alvarez, G.; Roca, A.G.; Nogués, J. Applications of exchange coupled bi-magnetic hard/soft and soft/hard magnetic core/shell nanoparticles. *Phys. Rep.* **2015**, *553*, 1–32. [[CrossRef](#)]
- Nogués, J.; Schuller, I.K. Exchange bias. *J. Magn. Magn. Mater.* **1999**, *192*, 203–232. [[CrossRef](#)]

7. Lottini, E.; López-Ortega, A.; Bertoni, G.; Turner, S.; Meledina, M.; Van Tendeloo, G.; De Julián Fernández, C.; Sangregorio, C. Strongly Exchange Coupled Core/Shell Nanoparticles with High Magnetic Anisotropy: A Strategy toward Rare-Earth-Free Permanent Magnets. *Chem. Mater.* **2016**, *28*, 4214–4222. [[CrossRef](#)]
8. Laureti, S.; Del Bianco, L.; Detlefs, B.; Agostinelli, E.; Foglietti, V.; Peddis, D.; Testa, A.M.; Varvaro, G.; Fiorani, D. Interface exchange coupling in a CoPt/NiO bilayer. *Thin Solid Films* **2013**, *543*, 162–166. [[CrossRef](#)]
9. Meiklejohn, W.H.; Bean, C.P. New magnetic anisotropy. *Phys. Rev.* **1957**, *105*, 904–913. [[CrossRef](#)]
10. Yang, M.; Ho, C.; Ruta, S.; Chantrell, R.; Krycka, K.; Hovorka, O.; Chen, F.; Lai, P.; Lai, C. Magnetic Interaction of Multifunctional Core–Shell Nanoparticles for Highly Effective Theranostics. *Adv. Mater.* **2018**, *30*, 1802444. [[CrossRef](#)]
11. Socoliuc, V.; Peddis, D.; Petrenko, V.I.; Avdeev, M.V.; Susan-Resiga, D.; Szabó, T.; Turcu, R.; Tombác, E.; Vékás, L. Magnetic Nanoparticle Systems for Nanomedicine—A Materials Science Perspective. *Magnetochemistry* **2019**, *6*, 2. [[CrossRef](#)]
12. Fabris, F.; Lohr, J.; Lima, E.; de Almeida, A.A.; Troiani, H.E.; Rodríguez, L.M.; Vásquez Mansilla, M.; Aguirre, M.H.; Goya, G.F.; Rinaldi, D.; et al. Adjusting the Néel relaxation time of Fe<sub>3</sub>O<sub>4</sub>/ZnCo<sub>1-x</sub>Fe<sub>2</sub>O<sub>4</sub> core/shell nanoparticles for optimal heat generation in magnetic hyperthermia. *Nanotechnology* **2021**, *32*, 065703. [[CrossRef](#)] [[PubMed](#)]
13. Estrader, M.; López-Ortega, A.; Golosovsky, I.V.; Estradé, S.; Roca, A.G.; Salazar-Alvarez, G.; López-Conesa, L.; Tobia, D.; Winkler, E.; Ardisson, J.D.; et al. Origin of the large dispersion of magnetic properties in nanostructured oxides: Fe<sub>x</sub>O/Fe<sub>3</sub>O<sub>4</sub> nanoparticles as a case study. *Nanoscale* **2015**, *7*, 3002–3015. [[CrossRef](#)] [[PubMed](#)]
14. Moon, S.H.; Noh, S.-H.; Lee, J.-H.; Shin, T.-H.; Lim, Y.; Cheon, J. Ultrathin Interface Regime of Core–Shell Magnetic Nanoparticles for Effective Magnetism Tailoring. *Nano Lett.* **2017**, *17*, 800–804. [[CrossRef](#)]
15. Muzzi, B.; Albino, M.; Innocenti, C.; Petrecca, M.; Cortigiani, B.; de Julián Fernández, C.; Bertoni, G.; Fernández-Pacheco, R.; Ibarra, A.; Marquina, C.; et al. Unraveling the mechanism of the one-pot synthesis of exchange coupled Co-based nano-heterostructures with high energy product. *Nanoscale* **2020**, *12*, 14076–14086. [[CrossRef](#)]
16. Quesada, A.; Granados-Miralles, C.; López-Ortega, A.; Erokhin, S.; Lottini, E.; Pedrosa, J.; Bollero, A.; Aragón, A.M.; Rubio-Marcos, F.; Stingaciu, M.; et al. Energy Product Enhancement in Imperfectly Exchange-Coupled Nanocomposite Magnets. *Adv. Electron. Mater.* **2016**, *2*, 1500365. [[CrossRef](#)]
17. Sun, S.; Zeng, H.; Robinson, D.B.; Raoux, S.; Rice, P.M.; Wang, S.X.; Li, G. Monodisperse MFe<sub>2</sub>O<sub>4</sub> (M=Fe, Co, Mn) Nanoparticles. *J. Am. Chem. Soc.* **2004**, *126*, 273–279. [[CrossRef](#)]
18. Omelyanchik, A.; Villa, S.; Vasilakaki, M.; Singh, G.; Ferretti, A.M.; Ponti, A.; Canepa, F.; Margaris, G.; Trohidou, K.N.; Peddis, D. Interplay between inter- and intraparticle interactions in bi-magnetic core/shell nanoparticles. *Nanoscale Adv.* **2021**. [[CrossRef](#)]
19. Muscas, G.; Singh, G.; Glomm, W.; Mathieu, R.; Kumar, P.A.; Concas, G.; Agostinelli, E.; Peddis, D. Tuning the Size and Shape of Oxide Nanoparticles by Controlling Oxygen Content in the Reaction Environment: Morphological Analysis by Aspect Maps. *Chem. Mater.* **2015**, *27*, 1982–1990. [[CrossRef](#)]
20. Bertotti, G. *Hysteresis in Magnetism*; Academic Press: Cambridge, MA, USA, 1998; pp. 3–30.
21. Concas, G.; Congiu, F.; Muscas, G.; Peddis, D. Determination of Blocking Temperature in Magnetization and Mössbauer Time Scale: A Functional Form Approach. *J. Phys. Chem. C* **2017**, *121*, 16541–16548. [[CrossRef](#)]
22. Micha, J.; Dieny, B.; Régnard, J.; Jacquot, J.; Sort, J. Estimation of the Co nanoparticles size by magnetic measurements in Co/SiO<sub>2</sub> discontinuous multilayers. *J. Magn. Magn. Mater.* **2004**, *272–276*, E967–E968. [[CrossRef](#)]
23. Knobel, M.; Nunes, W.C.; Socolovsky, L.M.; De Biasi, E.; Vargas, J.M.; DeNardin, J.C. Superparamagnetism and Other Magnetic Features in Granular Materials: A Review on Ideal and Real Systems. *J. Nanosci. Nanotechnol.* **2008**, *8*, 2836–2857. [[CrossRef](#)] [[PubMed](#)]
24. Livesey, K.L.; Ruta, S.; Anderson, N.R.; Baldomir, D.; Chantrell, R.W.; Serantes, D. Beyond the blocking model to fit nanoparticle ZFC/FC magnetisation curves. *Sci. Rep.* **2018**, *8*, 1–9. [[CrossRef](#)]
25. Bruvera, I.J.; Zélis, P.M.; Calatayud, M.P.; Goya, G.F.; Sánchez, F.H. Determination of the blocking temperature of magnetic nanoparticles: The good, the bad, and the ugly. *J. Appl. Phys.* **2015**, *118*, 184304. [[CrossRef](#)]
26. Omelyanchik, A.; Salvador, M.; D’orazio, F.; Mameli, V.; Cannas, C.; Fiorani, D.; Musinu, A.; Rivas, M.; Rodionova, V.; Varvaro, G.; et al. Magnetocrystalline and surface anisotropy in CoFe<sub>2</sub>O<sub>4</sub> nanoparticles. *Nanomaterials* **2020**, *10*, 1288. [[CrossRef](#)]
27. Peddis, D.; Orrù, F.; Ardu, A.; Cannas, C.; Musinu, A.; Piccaluga, G. Interparticle Interactions and Magnetic Anisotropy in Cobalt Ferrite Nanoparticles: Influence of Molecular Coating. *Chem. Mater.* **2012**, *24*, 1062–1071. [[CrossRef](#)]
28. El-Hilo, M.; Chantrell, R. Rationalisation of distribution functions for models of nanoparticle magnetism. *J. Magn. Magn. Mater.* **2012**, *324*, 2593–2595. [[CrossRef](#)]
29. Muscas, G.; Cobianchi, M.; Lascialfari, A.; Cannas, C.; Musinu, A.; Omelyanchik, A.; Rodionova, V.; Fiorani, D.; Mameli, V.; Peddis, D. Magnetic Interactions Versus Magnetic Anisotropy in Spinel Ferrite Nanoparticles. *IEEE Magn. Lett.* **2019**, *10*, 1–5. [[CrossRef](#)]
30. Mameli, V.; Musinu, A.; Ardu, A.; Ennas, G.; Peddis, D.; Niznansky, D.; Sangregorio, C.; Innocenti, C.; Thanh, N.T.K.; Cannas, C. Studying the effect of Zn-substitution on the magnetic and hyperthermic properties of cobalt ferrite nanoparticles. *Nanoscale* **2016**, *8*, 10124–10137. [[CrossRef](#)] [[PubMed](#)]
31. Peddis, D.; Laureti, S.; Mansilla, M.; Agostinelli, E.; Varvaro, G.; Cannas, C.; Fiorani, D. Exchange Bias in CoFe<sub>2</sub>O<sub>4</sub>/NiO nanocomposites. *Superlattices Microstruct.* **2009**, *46*, 125–129. [[CrossRef](#)]
32. Peddis, D.; Cannas, C.; Piccaluga, G.; Agostinelli, E.; Fiorani, D. Spin-glass-like freezing and enhanced magnetization in ultra-small CoFe<sub>2</sub>O<sub>4</sub> nanoparticles. *Nanotechnology* **2010**, *21*, 125705. [[CrossRef](#)]

33. Kodama, R.H.; Berkowitz, A.E.; McNiff, E.J.; Foner, S. Surface spin disorder in NiFe<sub>2</sub>O<sub>4</sub> nanoparticles. *Phys. Rev. Lett.* **1996**, *77*, 394–397. [[CrossRef](#)]
34. Oyarzún, S.; Tamion, A.; Tournus, F.; Dupuis, V.; Hillenkamp, M. Size effects in the magnetic anisotropy of embedded cobalt nanoparticles: From shape to surface. *Sci. Rep.* **2015**, *5*, 14749. [[CrossRef](#)]
35. Respaud, M.; Broto, J.M.; Rakoto, H.; Fert, A.R.; Thomas, L.; Barbara, B.; Verelst, M.; Snoeck, E.; Lecante, P.; Mosset, A.; et al. Surface effects on the magnetic properties of ultrafine cobalt particles. *Phys. Rev. B* **1998**, *57*, 2925–2935. [[CrossRef](#)]
36. Cabreira Gomes, R.; G da Silva, F.; Silva, T.-Q.; Gomide, G.; Pilati, V.; Aquino, R.; Geshev, J.; Perzynski, R.; Depeyrot, J. Magnetic irreversibility and saturation criteria in ultrasmall bi-magnetic nanoparticles. *J. Alloys Compd.* **2020**, *824*, 153646. [[CrossRef](#)]
37. Nogués, J.; Sort, J.; Langlais, V.; Skumryev, V.; Suriñach, S.; Muñoz, J.S.; Baró, M.D. Exchange bias in nanostructures. *Phys. Rep.* **2005**, *422*, 65–117. [[CrossRef](#)]
38. Omelianchik, A.; Singh, G.; McDonagh, B.H.; Rodionova, V.; Fiorani, D.; Peddis, D.; Laureti, S.; Omelyanchik, A. From Mn<sub>3</sub>O<sub>4</sub>/MnO core-shell nanoparticles to hollow MnO: Evolution of magnetic properties. *Nanotechnology* **2017**, *29*, 055703. [[CrossRef](#)] [[PubMed](#)]
39. Dai, J.; Feng, W.; Cheng, C.; Wen, X. The exchange bias effects of CoFe<sub>2</sub>O<sub>4</sub>@NiO nanofibers fabricated by electrospinning. *Mater. Res. Express* **2020**, *7*, 045009. [[CrossRef](#)]
40. Mohan, R.; Ghosh, M.; Mukherjee, S. The exchange bias effect in CoFe<sub>2</sub>O<sub>4</sub>/NiO nanocomposites prepared by chemical co-precipitation method. *Mater. Res. Express* **2019**, *6*, 056105. [[CrossRef](#)]
41. Chantrell, R.W.; O'Grady, K.; Search, H.; Journals, C.; Contact, A.; Iopscience, M.; Address, I.P. Magnetic characterization of recording media. *J. Phys. D. Appl. Phys.* **1992**, *25*, 1–23. [[CrossRef](#)]
42. García-Otero, J.; Porto, M.; Rivas, J. Henkel plots of single-domain ferromagnetic particles. *J. Appl. Phys.* **2000**, *87*, 7376. [[CrossRef](#)]
43. Wohlfarth, E.P. Relations between Different Modes of Acquisition of the Remanent Magnetization of Ferromagnetic Particles. *J. Appl. Phys.* **1958**, *29*, 595–596. [[CrossRef](#)]
44. Kelly, P.E.; O'Grady, K.; Mayo, P.I. Switching mechanisms in cobalt phosphorus thin films. In Proceedings of the International Magnetism Conference; IEEE: New York, NY, USA, 1989; Volume 25, p. HA5.
45. Wohlfarth, E.P. The coefficient of magnetic viscosity. *J. Phys. F Met. Phys.* **1984**, *14*, L155–L159. [[CrossRef](#)]
46. Laureti, S.; Varvaro, G.; Testa, A.M.; Fiorani, D.; Agostinelli, E.; Piccaluga, G.; Musinu, A.; Ardu, A.; Peddis, D. Magnetic interactions in silica coated nanoporous assemblies of CoFe<sub>2</sub>O<sub>4</sub> nanoparticles with cubic magnetic anisotropy. *Nanotechnology* **2010**, *21*, 315701. [[CrossRef](#)] [[PubMed](#)]
47. Chantrell, R.; Popplewell, J.; Charles, S. Measurements of particle size distribution parameters in ferrofluids. *IEEE Trans. Magn.* **1978**, *14*, 975–977. [[CrossRef](#)]
48. Bender, P.; Balceris, C.; Ludwig, F.; Posth, O.; Bogart, L.K.; Szczerba, W.; Castro, A.; Nilsson, L.; Costo, R.; Gavilán, H.; et al. Distribution functions of magnetic nanoparticles determined by a numerical inversion method. *New J. Phys.* **2017**, *19*, 073012. [[CrossRef](#)]
49. van Rijssel, J.; Kuipers, B.W.; Erné, B.H. Non-regularized inversion method from light scattering applied to ferrofluid magnetization curves for magnetic size distribution analysis. *J. Magn. Magn. Mater.* **2014**, *353*, 110–115. [[CrossRef](#)]
50. Huerta, J.M.M.; Medina, J.D.L.T.; Piroux, L.; Encinas, A. Self consistent measurement and removal of the dipolar interaction field in magnetic particle assemblies and the determination of their intrinsic switching field distribution. *J. Appl. Phys.* **2012**, *111*, 083914. [[CrossRef](#)]
51. Néel, L. Théorie du traînage magnétique des substances massives dans le domaine de Rayleigh. *J. Phys. Le Radium* **1950**, *11*, 49–61. [[CrossRef](#)]
52. Sandler, S.; Fellows, B.D.; Mefford, O.T. Best Practices for Characterization of Magnetic Nanoparticles for Biomedical Applications. *Anal. Chem.* **2019**, *91*, 14159–14169. [[CrossRef](#)]